Materials Science

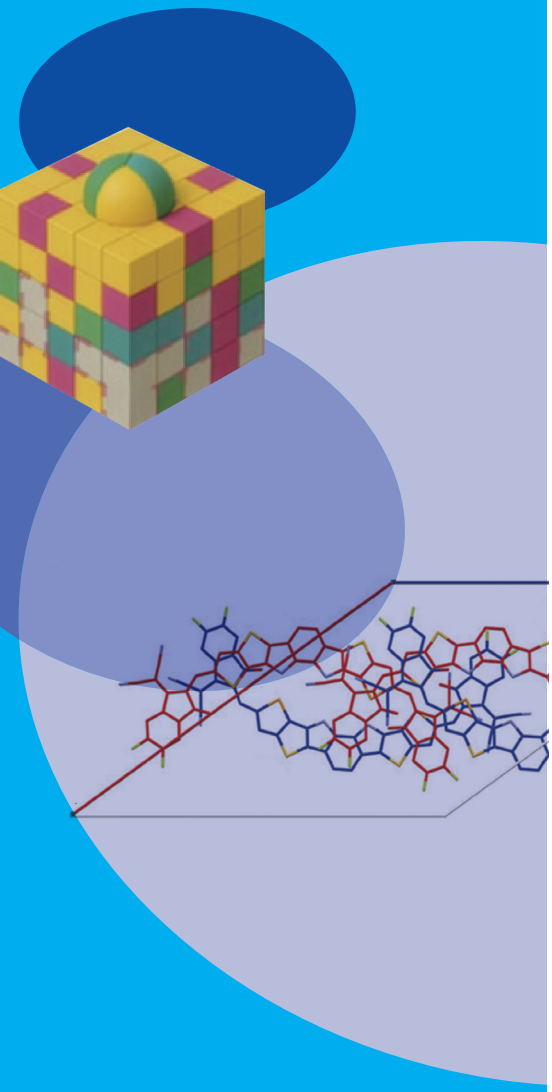

This section presents six articles that demonstrate how synchrotron radiation advances materials research by connecting structure, chemistry, and functionality across diverse material systems. The first article examines chiral perovskite nanoplates, using grazing-incidence X-ray scattering to resolve their layered structure and orientation in thin films. These structural insights are essential for understanding how chirality induces spin-polarized charge carriers, which enhance photocatalytic CO_2 reduction. The second article extends synchrotron analysis from soft semiconductors to metallic systems, using synchrotron nanodiffraction to map the phase stability of metastable β-tungsten films. By visualizing nanoscale phase distributions under realistic thermal conditions, this research elucidates how engineered interfaces support ultrafast and reliable spintronic memory devices.

Shifting toward molecular electronics, the third article demonstrates how grazing-incidence wide-angle X-ray scattering captures annealing-driven packing transitions in organic semiconductor thin films. This ability to directly observe the evolution toward single-crystal-like order explains why subtle changes in molecular arrangement can lead to significant improvements in charge mobility. Beyond static structure, synchrotron techniques are also critical for probing dynamic material behavior. This is exemplified in the fourth article, which investigates hybrid perovskites, where lattice dynamics blur the boundary between solid-like and liquid-like thermal transport. High-resolution diffraction and scattering measurements reveal the intimate coupling between molecular motion and phonon behavior, offering new insights into thermal management in functional materials.

As material complexity increases, element-specific information becomes essential. The fifth article demonstrates how X-ray absorption spectroscopy clarifies the roles of individual elements in high-entropy catalysts under operando conditions, identifying which metals actively drive redox reactions and which contribute to structural stability. The sixth study combines X-ray absorption spectroscopy (XAS), wide-angle X-ray scattering (WAXS), and X-ray excited optical luminescence to monitor phase evolution, defect states, and electronic structure in TiO_2 nanotube systems, facilitating the rational design of photoelectrochemical sensing platforms with biomedical applications. Together, these studies illustrate how synchrotron radiation enables systematic understanding and purposeful optimization of complex materials, underscoring its central role in modern materials science. (by Orion Shih)

Chirality-Regulated Spin Polarization of Perovskite Nanoplates for Photocatalytic CO_2 Reduction

The manipulation of spin-polarized electrons through chirality-regulated perovskite nanocrystals significantly enhances photocatalytic CO_2 reduction efficiency and highlights their strong potential for future solar-to-fuel conversion applications.

Artificial photosynthesis, which relies on solar-driven CO_2 reduction to generate high-value fuels, has recently attracted considerable attention as a promising approach to addressing both climate change and the global energy crisis. Among various strategies, photocatalytic CO_2 reduction has emerged as an especially appealing route, enabling the conversion of CO_2 into useful fuels and chemical feedstocks using renewable energy.[1] Chun-Wei Chen (National Taiwan University) and his collaborators demonstrate that photocatalytic CO_2 reduction efficiency can be markedly enhanced through chirality-regulated spin polarization in $CsPbBr_3$ perovskite nanocrystals.[2] Incorporating chiral molecules into layered perovskites provides an effective pathway to induce spin polarization, which in turn significantly boosts photocatalytic activity. Motivated by these insights, Chen and Chun-Jen Su (NSRRC) developed chirality-regulated perovskite thin films by introducing chiral organic molecules (MBA·Br) into all-inorganic $CsPbBr_3$ perovskite nanoplates (NPLs). This approach produces (R)- and (S)-two-dimensional (2D) Ruddlesden–Popper perovskite (RPP)/NPL hybrid structures. Within this hybrid configuration, the chiral 2D RPP domains impart strong chiroptical responses that facilitate the generation of spin-polarized electrons. As a result, chirality-induced spin polarization in these 2D RPP/NPL hybrid perovskite thin films effectively suppresses charge-carrier recombination, ultimately leading to a substantial enhancement in photocatalytic CO_2 reduction (CO_2RR) performance.

To elucidate the layered crystal structures of the synthesized materials, 2D grazing-incidence wide-angle X-ray scattering (2D-GIWAXS) measurements were conducted at the **TLS 23A1** beamline at the NSRRC. This technique enables comprehensive examination of crystallinity, phase composition, and lattice orientation in thin-film perovskite systems. As shown in **Fig. 1(d)**, the GIWAXS pattern of pristine $CsPbBr_3$ perovskite NPLs exhibits distinct

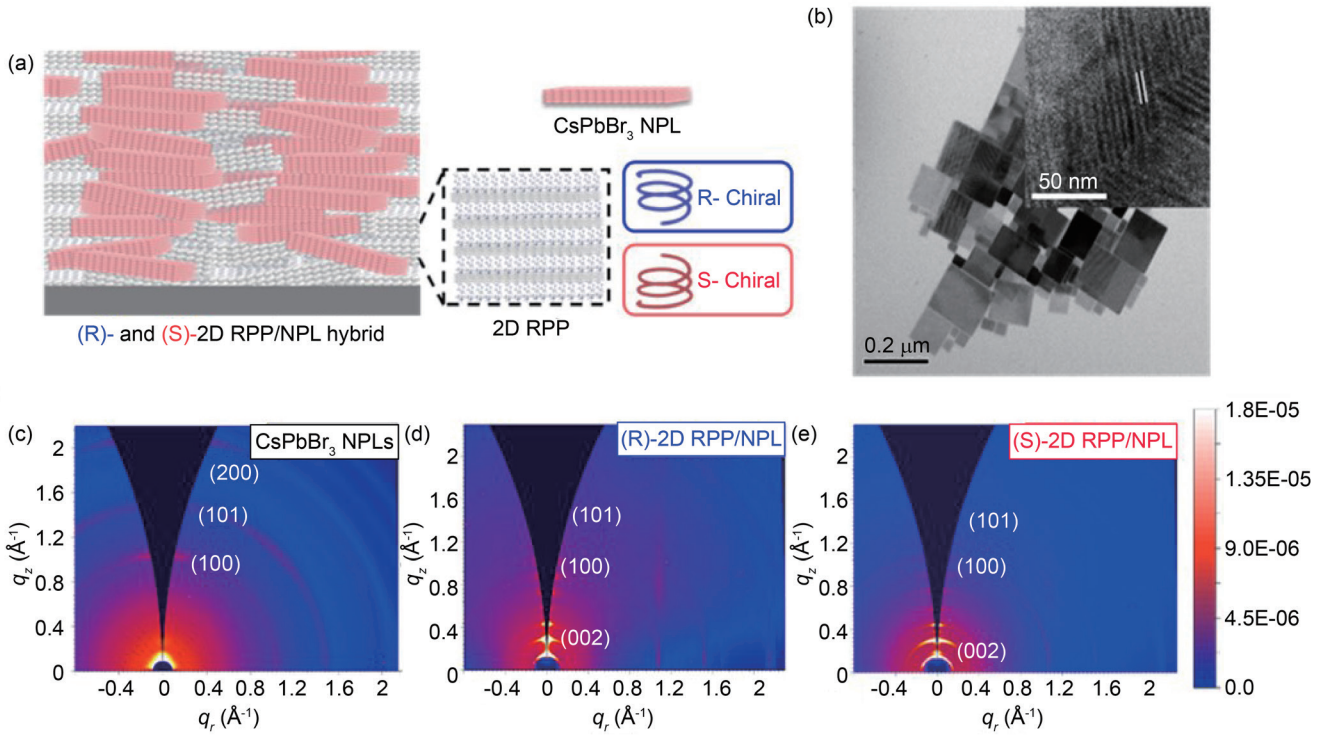

Fig. 1: Morphology and structural characterization of $CsPbBr_3$ perovskite NPLs, (R)-2D RPP/NPL, and (S)-2D RPP/NPL. (a) Schematic diagram of the (R)- and (S)-2D RPP/NPL hybrid perovskite thin films. (b) TEM image showing the morphology of $CsPbBr_3$ NPLs; the inset presents an HRTEM cross-sectional image of $CsPbBr_3$ NPLs. The 2D GIWAXS patterns of (c) $CsPbBr_3$ NPLs, (d) (R)-2D RPP/NPL, and (e) (S)-2D RPP/NPL. [Reproduced from Ref. 1]

diffraction features corresponding to the (100), (101), and (200) lattice planes. These peaks are characteristic signatures of the three-dimensional (3D) perovskite crystal structure, indicating that the $CsPbBr_3$ NPLs retain a crystallographic framework comparable to bulk 3D $CsPbBr_3$ perovskites. The results also confirm that the NPLs possess a highly anisotropic and layered morphology, with an ultrathin thickness of only a few nanometers, consistent with their nanoplate-like geometry. By contrast, the GIWAXS patterns of the (R)- and (S)-2D RPP/NPL hybrid $CsPbBr_3$ perovskite thin films—shown in **Figs. 1(d) and 1(e)**, respectively—display pronounced low scattering wavevector ($q < 1$ Å^{-1}) features. These low-q reflections are hallmarks of a 2D organic–inorganic hybrid RPP phase, confirming the incorporation of layered perovskite domains within the hybrid films. Notably, the (002) diffraction peak of the 2D RPP structure appears at $q = 0.16$ Å^{-1}, corresponding to an interlayer spacing of approximately 3.9 nm. This value closely matches the structural parameters of the $(MBA)_2Cs_3Pb_4Br_{13}$ perovskite (n = 4) phase. After accounting for the thickness of the organic chiral ligands, the thickness of the inorganic perovskite slabs is estimated to be ~3 nm, which is in good agreement with the cross-sectional High-Resolution Transmission Electron Microscopy (HRTEM) observations of $CsPbBr_3$ NPLs shown in the inset of **Fig. 1(b)**.

Furthermore, subtle but identifiable diffraction features at $q \approx 1.08$ Å^{-1} and 1.50 Å^{-1} in the hybrid films indicate the coexistence of 3D-like structural motifs within the predominantly 2D RPP–NPL architecture. These mixed-phase signatures suggest that the hybrid films consist of chiral 2D RPP layers embedded within or interfaced with the non-chiral $CsPbBr_3$ NPL matrix, forming a structurally integrated composite. Taken together, the GIWAXS results verify that our two-step synthesis protocol successfully produces both (R)- and (S)-2D RPP/NPL hybrid perovskite thin films with well-defined layered structures. Importantly, the embedded chiral RPP domains serve as key structural components responsible for transferring molecular chirality into the inorganic lattice, thereby generating spin-polarized charge carriers within the non-chiral perovskite NPL framework.

Circular dichroism (CD) and circularly polarized luminescence (CPL) reveal distinct chiroptical responses within the absorption and emission bands of the NPLs, indicating chirality transfer from the organic ligands to the inorganic layers (**Fig. 2**). Pristine $CsPbBr_3$ films show no CD signals, whereas hybrid R/S-2D RPP/NPL samples display pronounced signals, consistent with chiral-induced excitonic coupling within the metal-halide planes.

Under illumination, these chiral hybrid films show significantly improved photocatalytic CO_2RR performance (**Fig. 3**). The (R)- and (S)-2D RPP/NPL films achieve CO production rates of 45.5 and 30.6 μmol g^{-1}, respectively, substantially higher than the 15.1 μmol g^{-1} of pristine $CsPbBr_3$. Applying a 0.3 T external magnetic field further increases the CO yield to 75.3 and 49.3 μmol g^{-1},

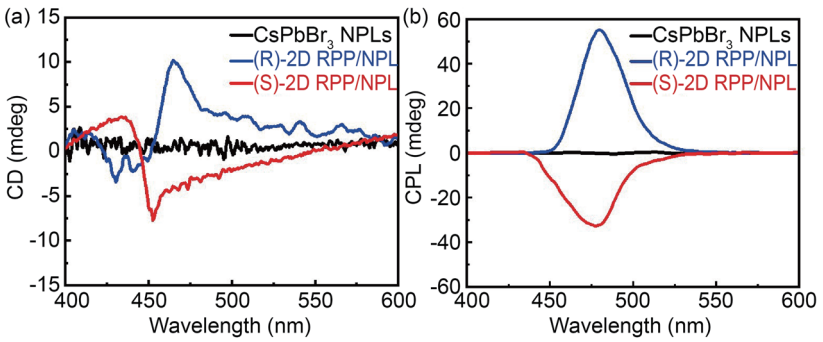

Fig. 2: (a) CD spectra of $CsPbBr_3$ NPLs, (R)-2D RPP/NPL, and (S)-2D RPP/NPL prepared using the two-step synthesis process. (b) CPL spectra of $CsPbBr_3$ NPLs, (R)-2D RPP/NPL, and (S)-2D RPP/NPL. [Reproduced from Ref. 1]

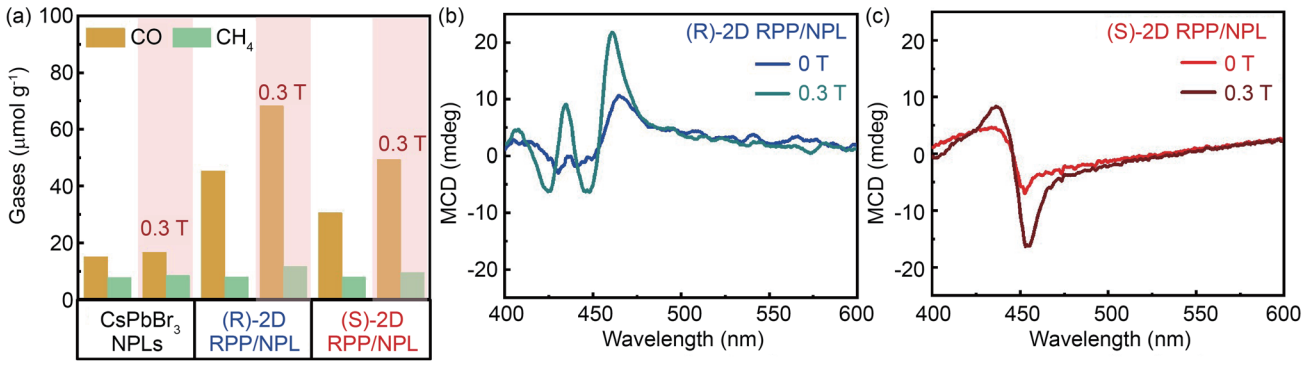

Fig. 3: The photocatalytic performance and MCD spectra of $CsPbBr_3$ NPLs, (R)-2D RPP/NPL, and (S)-2D RPP/NPL were evaluated with and without an external magnetic field (0.3 T). (a) Photocatalytic yield measurements for $CsPbBr_3$ NPLs, (R)-2D RPP/NPL, and (S)-2D RPP/NPL were conducted under irradiation for 6 hours, both with and without an external magnetic field (0 and 0.3 T). (b) and (c) show the MCD spectra of (R)-2D RPP/NPL and (S)-2D RPP/NPL, respectively, under both conditions (0 and 0.3 T). [Reproduced from Ref. 1]

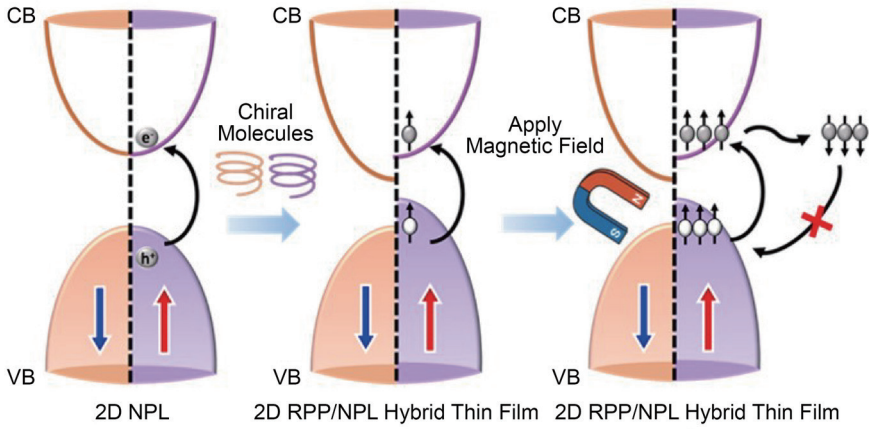

Fig. 4: Schematic illustration of the extended photoexcited carrier lifetime caused by electron spin polarization under an external magnetic field in chiral 2D RPP/NPL. [Reproduced from Ref. 1]

representing over a 60% improvement compared to zero-field conditions. This enhancement correlates with Zeeman splitting-induced amplification of spin-polarized electronic states, as confirmed by magnetic circular dichroism (MCD).

Figure 4 shows how spin-polarization control in chirality-regulated 2D RPP/NPL hybrid perovskite films enhances photocatalytic CO_2RR. In both (R)- and (S)-2D RPP/NPL hybrids, chirality transfer from chiral molecules induces spin-polarized band structures with asymmetric spin-up and spin-down density of states (DOS), unlike pristine $CsPbBr_3$ NPLs, which have symmetric DOS. Under illumination, photoexcited spin-polarized electrons typically undergo spin relaxation due to strong spin–orbit coupling and hyperfine interactions; however, carrier recombination is suppressed because spin-polarized holes of matching orientation in the valence band are limited. This extends carrier lifetimes and improves CO_2RR efficiency in the chiral hybrids. An external magnetic field introduces additional Zeeman splitting, increasing spin-polarized carrier populations and further prolonging lifetimes. This mechanism demonstrates the link between spin polarization control in chirality-regulated 2D RPP/NPL hybrid perovskite thin films and enhanced photocatalytic CO_2RR.

This work demonstrates that chirality-induced spin polarization effectively suppresses recombination and promotes charge transfer in perovskite photocatalysts. Coupling this approach with external magnetic fields further enhances CO_2-to-fuel conversion efficiency, suggesting a promising direction for high-performance solar-to-fuel platforms. (Reported by Chun-Wei Chen, National Taiwan University)

This report features the work of Chun-Wei Chen and his collaborators published in J. Am. Chem. Soc. ***147****, 40347 (2025).*

TLS 23A1 Small/Wide Angle X-ray Scattering

- GIWAXS
- Materials Science, Chemistry, Material Structure

References

1. C.-C. Lin, S.-K. Huang, W.-N. Tseng, C.-J. Su, C.-C. Huang, C.-Y. Huang, C.-Y. Yu, M.-H. Lai, J.-Y. Sun, Y.-C. Chao, H.-S. Hsu, C.-W. Luo, Y.-M. Chang, C.-C. Chen, C.-W. Chen, J. Am. Chem. Soc. **147**, 40347 (2025).
2. C.-C. Lin, T.-R. Liu, S.-R. Lin, K. M. Boopathi, C.-H. Chiang, W.-Y. Tzeng, W.-H. C. Chien, H.-S. Hsu, C.-W. Luo, H.-Y. Tsai, H.-A. Chen, P.-C. Kuo, J. Shiue, J.-W. Chiou, W.-F. Pong, C.-C. Chen, C.-W. Chen, J. Am. Chem. Soc. **144**, 15718 (2022).

Thermally Stable β-Tungsten for 64-kb SOT-MRAM: Structural Stability Revealed by Synchrotron Nanodiffraction

1-nanosecond magnetic memory breakthrough moves MRAM closer to mass production.

Modern computing systems rely heavily on charge-based memory subsystems, including static random-access memory (SRAM), dynamic random-access memory (DRAM), and flash memory.[1] However, as these technologies scale beyond the 10-nm node, they face significant physical challenges, specifically performance degradation, reliability concerns, and read/write disturbances. To overcome these challenges, emerging non-volatile memory technologies, such as spin–orbit torque magnetic random-access memory (SOT-MRAM), spin-transfer torque magnetic random-access memory (STT-MRAM), and phase-change memory (PCM), are being developed. These technologies provide low latency, reduced power consumption, and seamless integration with complementary metal-oxide-semiconductor (CMOS) technology. Among these options, SOT-MRAM is especially suitable to replace cache-level SRAM due to its rapid write speeds and high energy efficiency. By using materials with strong spin-orbit coupling (SOC), SOT-MRAM can switch the magnetization of magnetic tunnel junctions (MTJs) with high reliability. Additionally, its three-terminal architecture separates read and write paths, addressing the endurance limitations in STT-MRAM.

Tungsten (W) is a leading material for SOT applications because of its high SOC. Specifically, tungsten in its β-phase (A15 structure) exhibits a large spin-Hall angle of approximately -0.4 to -0.6, facilitating excellent switching efficiency. However, β-W is metastable and tends to transform into the thermodynamically stable α-phase, which has a negligible spin-Hall angle, when the film thickness exceeds 5 nm or during back-end-of-line (BEOL) annealing at 400°C.[2] This creates a significant integration conflict: although thick W layers are necessary to ensure a robust etching process and high yield, they also increase the risk of phase transformation.

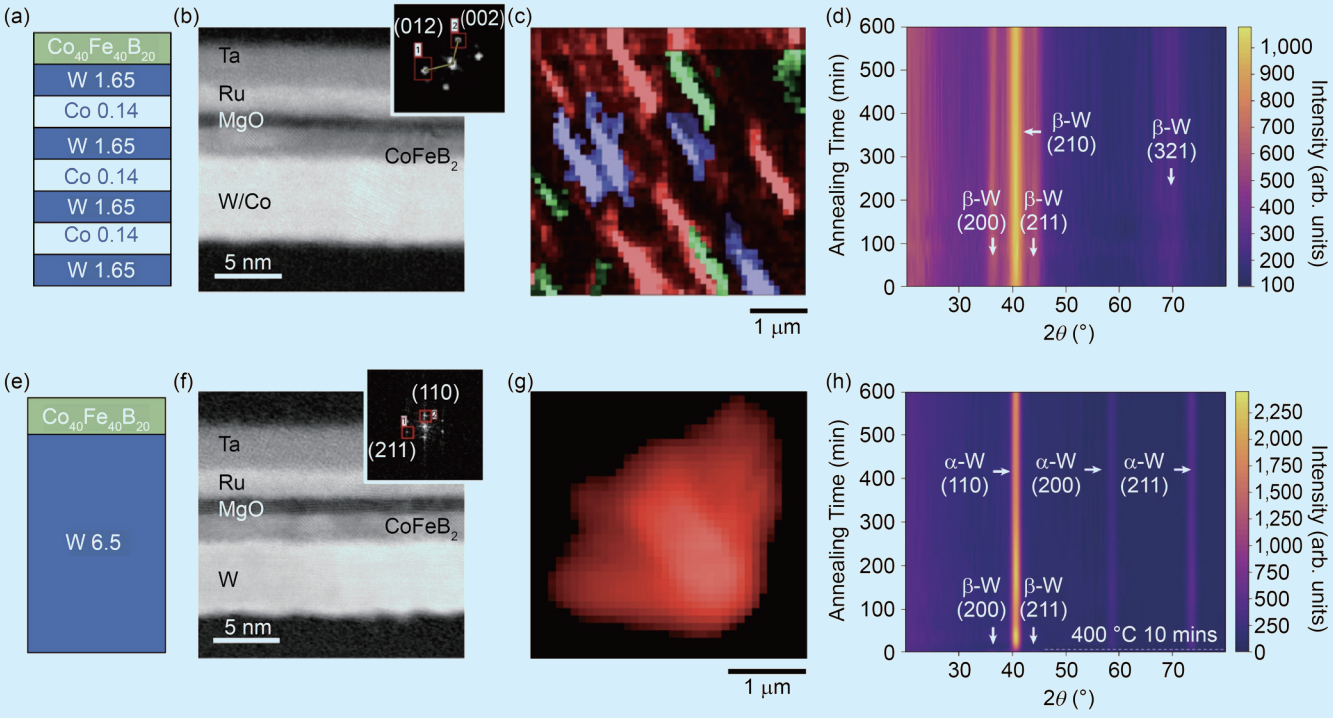

Fig. 1: Structural stability of composite-W. (a–d) The composite-W film incorporates Co insertion layers to maintain the β-W phase, as confirmed by transmission electron microscopy and grazing incidence X-ray diffraction. (c) Synchrotron nanodiffraction mapping (**TPS 21A**) reveals field-aligned β-W crystalline grains. (e–h) Single-layer W undergoes a full phase transformation to α-W under identical annealing conditions (400 °C). [Reproduced from Ref. 3]

In this study, Yen-Lin Huang's (National Yang Ming Chiao Tung University) team presents a cobalt (Co) insertion layer design that successfully stabilizes the β-W phase, which is revealed by the high-resolution X-ray nanodiffraction at **TPS 21A** at the NSRRC, even under stringent BEOL thermal constraints. This composite approach enables the creation of thick W layers that maintain high thermal stability and a record spin-Hall conductivity of approximately 4,500 $\Omega^{-1}cm^{-1}$.[3]

Synchrotron-Based Phase Characterization

To address this stability challenge, the team developed a composite-W structure incorporating thin cobalt insertion layers that serve as diffusion barriers. The critical evidence for the phase stability of this design was obtained through high-resolution X-ray nanodiffraction at **TPS 21A** at the NSRRC.

Using a monochromatic X-ray beam focused on a 90 × 90 nm^2 spot, the team performed spatial diffraction mapping to identify the distribution of W phases. As shown in **Fig. 1(c)**, the nanodiffraction maps revealed that the composite-W film maintains a robust, crystallized β-phase after annealing. Notably, we observed distinct stripy crystal features aligned with the direction of the annealing field, suggesting a symmetry-breaking effect potentially beneficial for field-free switching. In contrast, single-layer W films without Co insertion underwent complete transformation into the stable α-phase after only 10 minutes at 400 °C. These results demonstrate that our composite design can withstand 400 °C for up to 10 hours and even 700 °C for 30 minutes, meeting the most stringent BEOL thermal budgets.

64-kb SOT-MRAM Performance

Leveraging the stabilized β-W spin-current source, the team successfully integrated a 64-kilobit SOT-MRAM array using a standard CMOS process.

The device characterization presented in **Fig. 2** highlights the exceptional performance of the composite-W integration.

- High Read Margin: The magnetic tunnel junctions exhibit a tunneling magnetoresistance of approximately 146%, ensuring reliable data readout.
- Ultrafast Switching: The 64-kb chip demonstrates reliable SOT switching at speeds as fast as 1 ns.
- Long-Term Reliability: The team extracted a thermal stability factor (Δ) of approximately 116, corresponding to a data retention period exceeding 10 years.
- Field-Free Operation: The symmetry-breaking properties identified in the synchrotron maps enabled field-free switching, which is critical for simplifying high-density memory architectures.

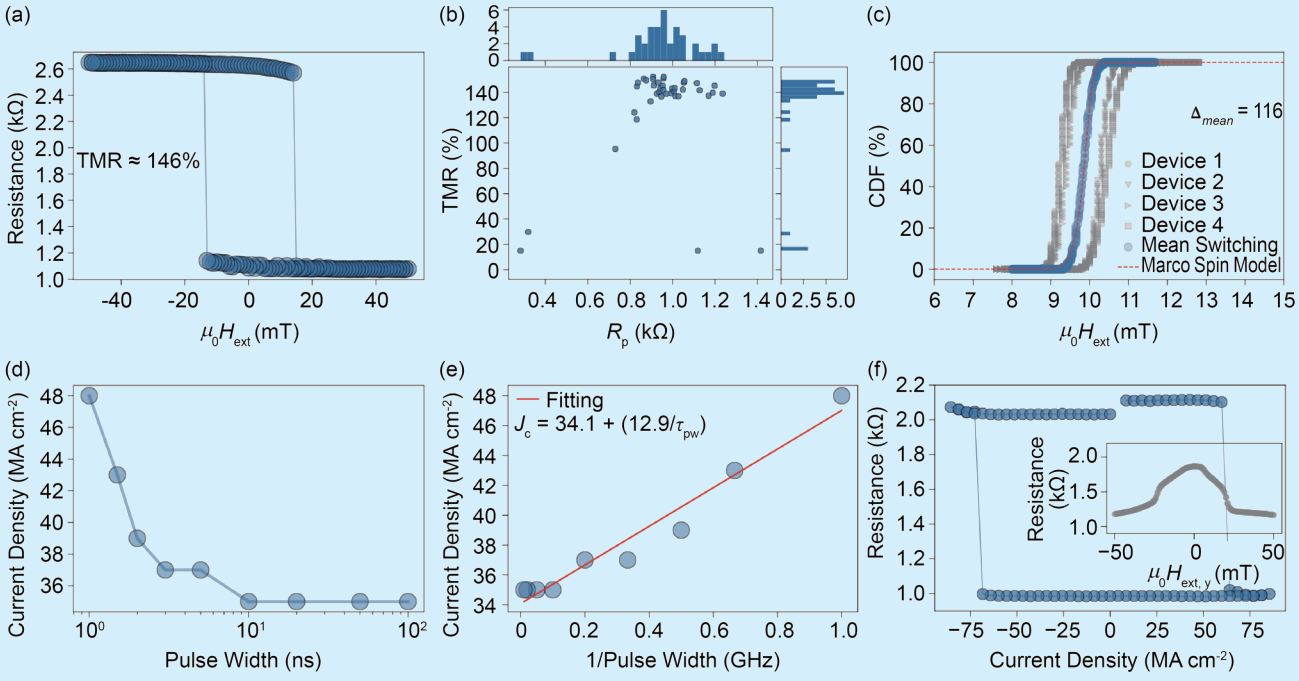

Fig. 2: 64-kb SOT-MRAM characterization. (a–b) The integrated MTJ exhibits a TMR of ~146%. (c–e) Statistical analysis of 8,000 devices shows a thermal stability (Δ) of 116 and successful 1 ns switching at high current densities. (f) Evidence of field-free switching due to the symmetry-breaking design of the composite W. [Reproduced from Ref. 3]

Conclusion

By combining innovative material engineering with advanced synchrotron analysis at the NSRRC, the team has demonstrated a BEOL-compatible SOT-MRAM solution that overcomes a major roadblock for commercial semiconductor integration. This work underscores the vital role of nanodiffraction techniques in characterizing next-generation spintronic materials. (Reported by Yen-Lin Huang, National Yang Ming Chiao Tung University)

This report features the work of Yen-Lin Huang and his collaborators published in Nat. Electron. ***8****, 794 (2025).*

TPS 21A X-ray Nanodiffraction

- n-XRD, ED-XND
- Materials Science, Electronic Device, Microstructural Domain Image

References

1. H.-S. P. Wong, S. Salahuddin, Nat. Nanotechnol. **10**, 191 (2015).
2. C.-F. Pai, L. Liu, Y. Li, H. W. Tseng, D. C. Ralph, R. A. Buhrman, Appl. Phys. Lett. **101**, 122404 (2012).
3. Y.-L. Huang, M. Song, C.-M. Lee, Y.-W. Chen, C.-Y. Chiang, S.-H. Chou, L.-C. Hsu, H.-J. Liu, G.-L. Chen, S.-Y. Yang, Y.-J. Chang, I-J. Wang, Y.-C. Hsin, Y.-H. Su, J.-H. Wei, F. Xue, S. X. Wang, X. Bao, Nat. Electron. **8**, 794 (2025).

Highly Crystalline Selenium-Substituted Acceptor-Donor-Acceptor-Type Acceptor Enabling High-Mobility N-Type Transistors

Selenium-substituted non-fullerene acceptor CB-2Se exhibits a single-crystal-like thin-film packing after thermal annealing, resulting in exceptional n-type organic field-effect transistor mobility of 1.18 $cm^2 V^{-1} s^{-1}$ with excellent air stability.

In 2019, the non-fullerene acceptor (NFA) material Y6 emerged as a groundbreaking development in organic solar cells, achieving a power conversion efficiency of 15.7%.[1] This milestone significantly advanced the development of organic photovoltaic (OPV) materials. Y6 features an A-$D_N A'_N$D-A-type molecular architecture with a characteristic C-shaped geometry, incorporating an electron-deficient thiodiazole (Tz, A′ unit) into the core. This structural motif effectively modulates intermolecular interactions and molecular packing. Recently, a structurally simplified A-$D_N B_N$D-A NFA, CB16, was developed, employing an unsubstituted *ortho*-benzodipyrrole (*o*-BDP) core derived from Y6 by removing the A′ moiety.[2] Both CB16 and Y6 derivatives share a key structural feature: the *o*-BDP core. This semi-circular, π-conjugated unit facilitates the formation of three-dimensional interpenetrated networks through self-assembly, promoting multidirectional charge transport pathways. As a result, inverted OPVs based on CB16 achieved efficiencies comparable to those of Y-series materials. Ongoing structural refinement of CB-based architectures is expected to drive the advancement of next-generation acceptor–donor–acceptor-type (A–D–A-type) NFAs.

Despite the rapid progress of OPV technologies, NFAs have yet to demonstrate high electron mobility in organic field-effect transistors (OFETs). To date, the development of n-type OFETs remains limited, particularly for solution-processable systems under ambient conditions. Key challenges include the suboptimal molecular ordering and stacking behavior of NFAs, which restrict their charge-transport capabilities. Reports of n-type OFETs with electron mobilities exceeding 1 $cm^2 V^{-1} s^{-1}$ remain scarce, and such performance is typically observed only in single-crystal devices—systems that are difficult to fabricate and scale, thus limiting their practical applicability. Therefore, there is an urgent need to design new NFAs that can self-assemble into highly crystalline, single-crystal-like domains in thin films *via* solution processing. However, rational design strategies for such materials remain underdeveloped. Notably, C-shaped NFAs based on the *o*-BDP core exhibit extensive π–π interactions in the solid state, enabling the formation of interpenetrating three-dimensional networks. These networks provide diverse charge transport pathways, underscoring their potential for single-component OFET applications.

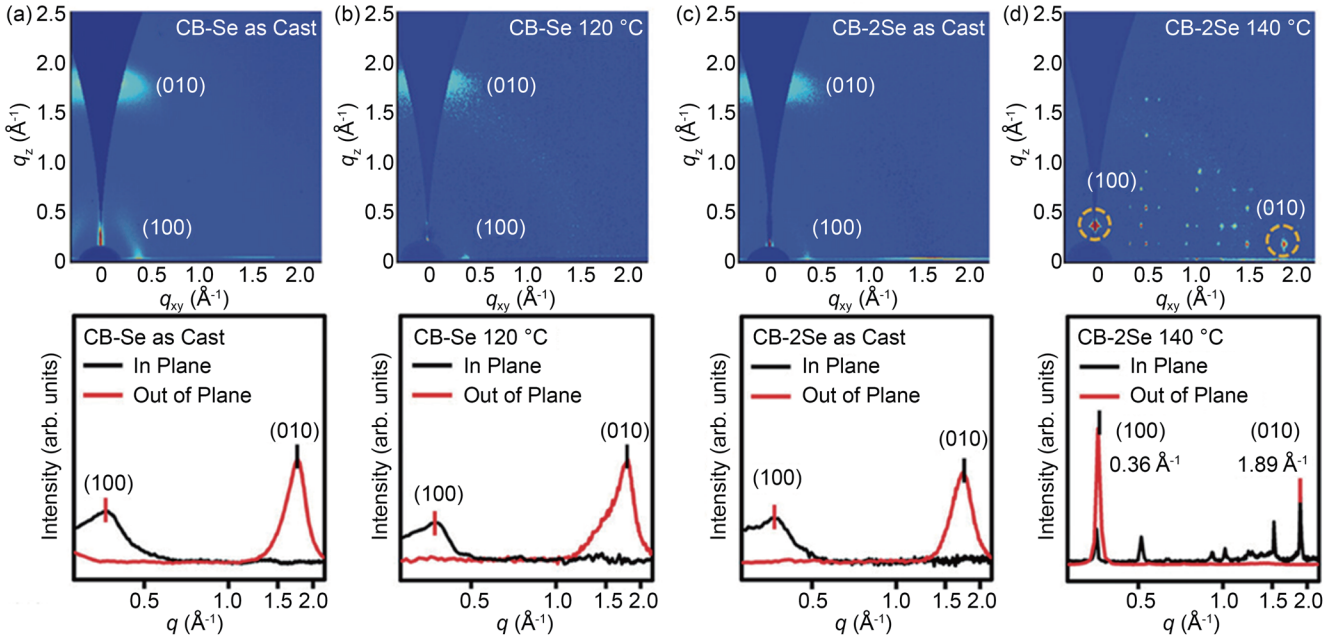

Fig. 1: Two-dimensional GIWAXS patterns of (a) as-cast CB-Se and (b) CB-Se neat film thermally annealed at 120 °C for 10 min; (c) as-cast CB-2Se and (d) CB-2Se neat film thermally annealed at 140 °C for 10 min, showing the appearance of highly oriented diffraction peaks. [Reproduced from Ref. 3]

Recently, Yen-Ju Cheng's team (National Yang Ming Chiao Tung University) implemented a selenium-substitution (Se-substitution) strategy on the central D_NB_ND ladder-π-core, yielding asymmetric CB-Se and symmetric CB-2Se. Due to the higher polarizability of Se atoms, introducing a selenophene unit into organic semiconductors has proven to be an effective strategy for strengthening intermolecular Se-Se or Se-π interactions. These features enhance the crystallinity of the NFAs and promote the formation of single-crystal molecular assemblies, thereby enabling excellent ambipolar OFET performance. Notably, the symmetric CB-2Se exhibited an outstanding electron mobility of 1.18 cm^2 V^{-1} s^{-1} and a hole mobility of 0.63 cm^2 V^{-1} s^{-1} in the OFET device, along with exceptional air stability.

To elucidate the molecular packing and film morphology of the two NFAs, grazing-incidence wide-angle X-ray scattering (GIWAXS) measurements were conducted at **TPS 25A** (**Fig. 1**) with experimental assistance from Yi-Wei Tsai, Jhih-Ming Lin, and U-Ser Jeng from the NSRRC. The as-cast neat films of CB-Se and CB-2Se exhibited pronounced (010) diffraction peaks in the out-of-plane direction and broad (100) refractions in the in-plane direction, indicative of a predominantly face-on orientation. When both NFAs were subjected to thermal annealing for 10 min, CB-Se still showed a face-on orientation. However, the initially arc-like diffraction pattern of the as-cast CB-2Se film was converted into a discrete point-like pattern, indicating the formation of highly crystalline packing. CB-2Se displayed a distinct (010) peak at q_{xy} = 1.89 Å^{-1} in the in-plane direction, indicating that thermal annealing induced a transition from a face-on to an edge-on orientation, along with a pronounced reduction in the π–π stacking distance from 3.59 to 3.32 Å. Correspondingly, an intense (100) peak emerged at q_z = 0.36 Å^{-1} in the out-of-plane direction, indicating an expanded lamellar spacing of 17.49 Å. In addition, the coherence lengths of both the (100) and (010) peaks were estimated to be 39.6 nm and 18.5 nm, respectively, indicating larger crystalline domain sizes. These features facilitated charge transport in the OFET device and minimized the presence of grain boundaries, resulting in outstanding electron mobility and air stability. The major GIWAXS diffraction peaks of the thermally annealed CB-2Se thin film, particularly those at q_z = 0.36 Å^{-1} and q_{xy} = 1.89 Å^{-1}, closely coincided with the corresponding peaks (0.35 Å^{-1} and 1.86 Å^{-1}) in the simulated single-crystal patterns, demonstrating that the CB-2Se film exhibited single-crystal-like characteristics. To simulate the molecular packing in the CB-2Se thin film further, I-Jui Hsu's team (National Taipei University of Technology) extracted the 1D scattering line-cut profiles in the q_{xy} and q_z directions from **Fig. 1(d)** and indexed them using typical powder X-ray diffraction programs, N-TREOR and DICVOL in the Expo2014 package. The simulated unit-cell packing model (**Fig. 2(a)**, see next page), along with the b-axis view (**Fig. 2(b)**), showed that CB-2Se molecules adopted an edge-on π–π stacking orientation along the b-axis on the substrate surface. Within the unit cell, two distinct dimeric arrangements emerged: an M-shaped core-to-terminal (CT) π–π stacking and an S-shaped CT–CT mode, both exhibiting tight π–π stacking distances—3.38 and 3.35 Å, respectively (**Fig. 2(c)**). Upon thermal annealing (**Fig. 2(d)**), the solution-processed CB-2Se film transformed from a kinetically trapped face-on configuration to a thermodynamically favored edge-on packing. This single-crystal-like arrangement, characterized by an edge-on orientation and an enlarged lateral coherence

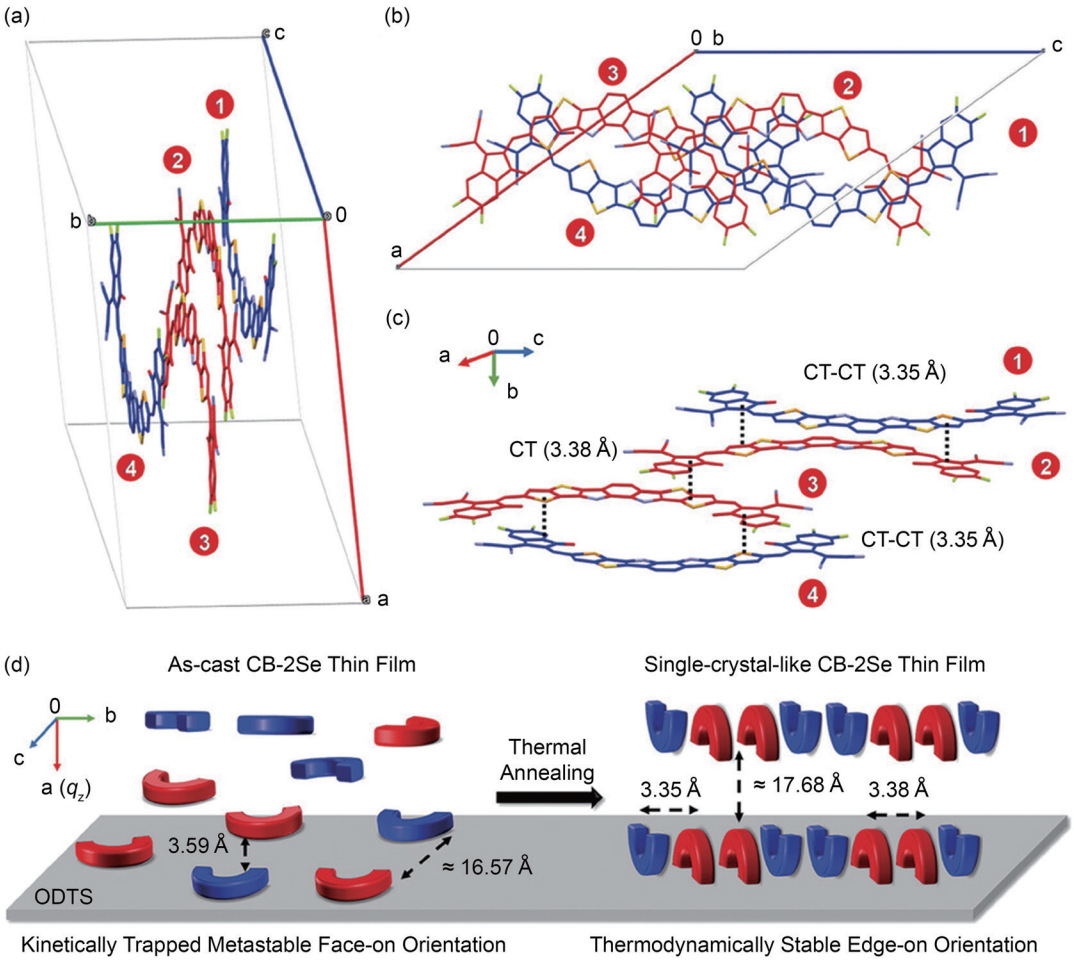

Fig. 2: (a) Simulated packing model in a unit cell of the thermally annealed CB-2Se thin film on the substrate (bc-face); (b) packing structure viewed along the b-axis; (c) side view showing the π–π distances of the dimeric CT and CT–CT modes; (d) illustration of the thermally induced transformation of the CB-2Se thin film from a face-on to an edge-on packing structure on the substrate. [Reproduced from Ref. 3]

length, effectively reduced grain boundaries and thereby lowered the trap density.

In summary, Se-substituted and symmetric NFA CB-2Se, with strong intermolecular interactions, enables the development of a single-crystal-like, solution-processed thin film that transitions from a kinetically trapped face-on π–π stacking orientation to a thermodynamically stable edge-on configuration upon thermal annealing. The CB-2Se-based OFET device achieved a remarkable electron mobility of 1.18 $cm^2 V^{-1} s^{-1}$ with exceptional n-type air stability, outperforming the corresponding A-D_NA′$_N$D-A-type Y6-based materials by two orders of magnitude and representing the highest reported value for solution-processed n-type OFETs utilizing A–D–A-type small molecules. (Reported by Yen-Ju Cheng, National Yang Ming Chiao Tung University)

This report features the work of Yen-Ju Cheng and his collaborators published in Adv. Funct. Mater. ***35****, 2419176 (2025).*

TPS 25A Coherent X-ray Scattering

- GIWAXS
- Materials Science, Organic Semiconductor

References

1. J. Yuan, Y. Zhang, L. Zhou, G. Zhang, H.-L. Yip, T.-K. Lau, X. Lu, C. Zhu, H. Peng, P. A. Johnson, M. Leclerc, Y. Cao, J. Ulanski, Y. Li, Y. Zou, Joule **3**, 1140 (2019).
2. Y.-J. Xue, Z.-Y. Lai, H.-C. Lu, J.-C. Hong, C.-L. Tsai, C.-L. Huang, K.-H. Huang, C.-F. Lu, Y.-Y. Lai, C.-S. Hsu, J.-M. Lin, J.-W. Chang, S.-Y. Chien, G.-H. Lee, U.-S. Jeng, Y.-J. Cheng, J. Am. Chem. Soc. **146**, 833 (2024).
3. K.-H. Huang, C.-C. Tseng, C.-L. Tsai, Y.-J. Xue, H.-C. Lu, C.-F. Lu, Y.-Y. Chang, C.-L. Huang, I. Hsu, Y.-Y. Lai, Y.-P. Zheng, B.-H. Jiang, C.-P. Chen, S.-Y. Chien, U. Jeng, C.-S. Hsu, Y.-J. Cheng, Adv. Funct. Mater. **35**, 2419176 (2025).

The Mystery of Hybrid Perovskites: Why Some Crystals Act Like Both Solids and Liquids

From dual incommensurate phases in $MAPbBr_3$ to crystal-liquid thermal transport in $MAPbCl_3$, organic cation rotation emerges as the key control parameter.

Hybrid organic–inorganic perovskites, with the general formula $MAPbX_3$ (MA = methylammonium, X = halide), have emerged as revolutionary materials for solar cell applications, achieving power conversion efficiencies above 25%.[1] However, the fundamental mechanisms underlying their exceptional optoelectronic properties remain unclear. The interaction between rotatable organic cations and the dynamically disordered inorganic framework generates a complex phonon landscape that traditional characterization techniques cannot readily resolve.

To address this challenge, researchers from National Central University and National Cheng Kung University employed X-ray and neutron diffraction and inelastic neutron scattering instruments at both NIST **SPINS** and Australian Nuclear Science and Technology Organisation's **SIKA** to investigate the atomic-scale dynamics of $MAPbBr_3$ and $MAPbCl_3$ single crystals. Neutron scattering was essential for this investigation. Unlike X-rays, which primarily probe electron density, neutrons interact directly with atomic nuclei and are especially sensitive to hydrogen—a key component of the MA^+ cations. This sensitivity enables neutrons to map the orientational disorder and rotational dynamics of organic molecules buried within the dense PbX_6 octahedral framework. Furthermore, inelastic neutron scattering directly measures phonon energies and lifetimes across the entire Brillouin zone, providing a complete picture of how heat-carrying vibrations propagate through both the rigid inorganic lattice and the mobile organic sublattice.

Building on earlier observations of an incommensurate phase in $MAPbBr_3$,[2] Wen-Hsien Li's team at National Central University discovered that this complexity extends to dual incommensurate phases persisting across a much broader temperature range using neutron diffraction data.[3] Two distinct phases coexist below 150 K: a low-temperature phase (ICM_{LT}) that remains stable down to 75 K, and a high-temperature phase (ICM_{HT}) appearing between 134 and 150 K. Remarkably, the transition between these phases induces extremely large lattice distortions—a 0.25% contraction followed by a 0.42% expansion of the tetragonal basal plane within just 9 K. These structural changes arise from the reorientation of MA^+ ions, which form an incommensurate sublattice with spatial periodicity different from the $PbBr_3^-$ framework.

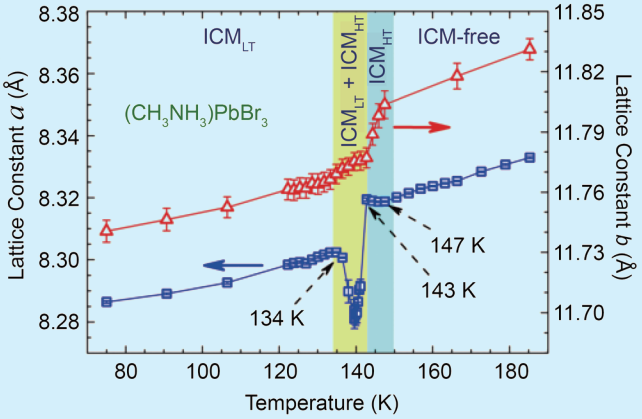

Fig. 1: Temperature dependencies of the lattice constants *a* (open squares) and *b* (open triangles). Large negative thermal expansions followed by large positive thermal expansions are seen for *a* in the regime where ICM_{LT} and ICM_{HT} coexist (yellow shaded region). Large positive thermal expansion of *b* in the ICM_{HT}-solely regime (blue shaded region) is also visible. [Reproduced from Ref. 3]

Phonon dispersion measurements at 75 K revealed six definitive acoustic-like phonon branches in $MAPbBr_3$, indicating that the MA^+ sublattice is solid enough to support its own vibrational modes. Upon warming to 200 K, these six branches reconstruct into just two, with significantly enhanced frequencies. This phonon reconstruction reflects the thermal disordering of MA^+ ions, which progressively reduces the degree of atomic disorder in the $PbBr_3^-$ framework—a counterintuitive effect where heating actually improves lattice perfection.

The investigation of $MAPbCl_3$ by Pai-Chun Wei's team (National Cheng Kung University) uncovered an even more striking phenomenon: dual crystal-liquid thermal transport behavior.[4] The team employs high-resolution powder X-ray diffraction at **TPS 19A**. The result shows that below 168.9 K in the orthorhombic phase, $MAPbCl_3$ exhibits crystal-like thermal conductivity that decreases with temperature—typical for crystalline solids dominated by phonon-phonon scattering. However, upon transitioning to the cubic phase above 174.8 K, thermal conductivity begins to increase with temperature, resembling the behavior of liquids or gases where enhanced molecular motion improves heat transfer.

This unusual transition is driven by the onset of rotational jumps in MA^+ cations, which shift the lattice distortion

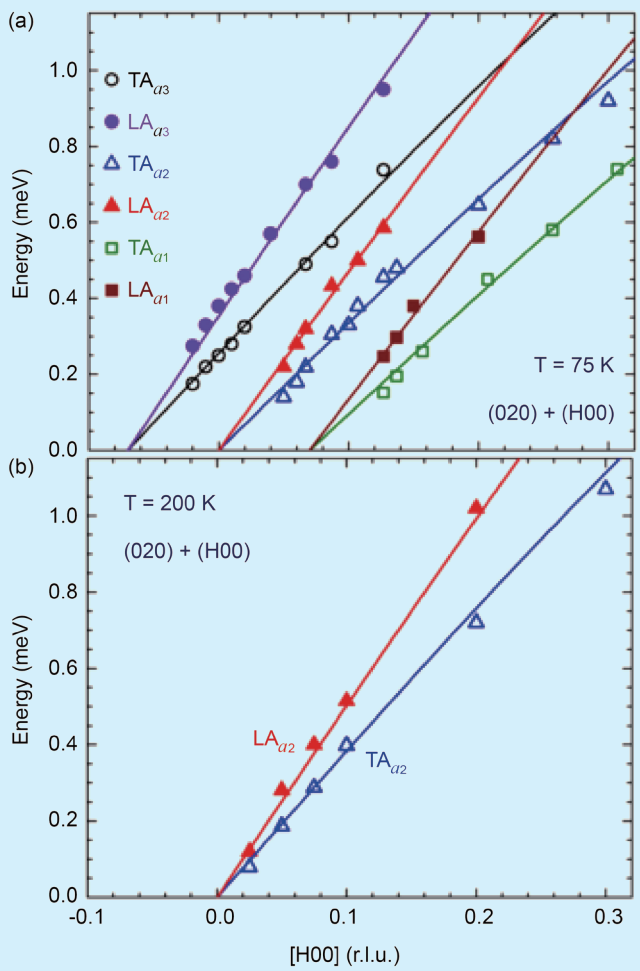

Fig. 2: Phonon dispersion curves of $(CH_3NH_3)PbBr_3$ along the [H00] crystallographic direction at (a) 75 K and (b) 200 K. The solid curves show the results of fitting the data to harmonic expressions, as discussed in the text. Six phonon branches are present at 75 K, grouped as follows: two branches originate from the zone center at H = 0, labeled LA_{a2} (solid triangles) and TA_{a2} (open triangles); two originate from H = 0.07, labeled LA_{a1} (solid squares) and TA_{a1} (open squares); and two originate from H = –0.07, labeled LA_{a3} (solid circles) and TA_{a3} (open circles). At 200 K, the four ICM branches disappear, while the two CM branches remain. [Reproduced from Ref. 3]

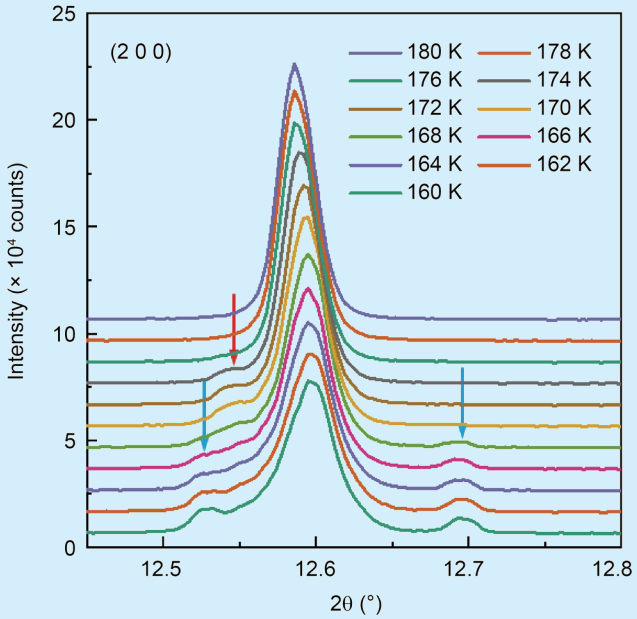

Fig. 3: Evolution of the (2 0 0) diffraction peak during phase transitions. [Reproduced from Ref. 4]

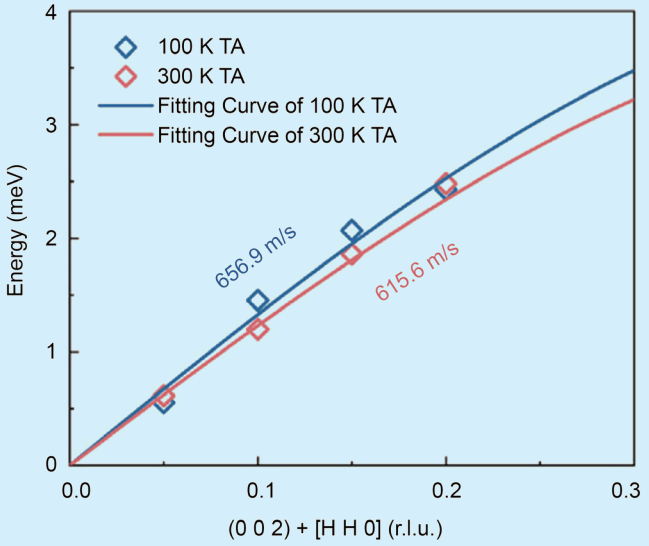

Fig. 4: Phonon dispersion relations in $MAPbCl_3$ measured at 100 K and 300 K: Transverse acoustic (TA) phonon dispersions along the [H H 0] direction. [Reproduced from Ref. 4]

from a static to a dynamic regime. Using the **SIKA** spectrometer, the team measured exceptionally low phonon velocities (656.9 m/s for transverse acoustic modes at 100 K) and ultrashort phonon lifetimes (0.788–8.67 ps at 300 K). The phonon mean free paths approach the Regel-Ioffe limit of just 5–10 Å—comparable to the Pb–Cl bond length itself—indicating that phonons are scattered so frequently that they can barely propagate.

The combination of low phonon velocities, short lifetimes, and minimal mean free paths leads to thermal conductivity near the theoretical amorphous limit (0.211 W/m·K) over a wide temperature range. This ultralow thermal conductivity is lower than that of well-known thermoelectric materials such as SnSe and GeTe, demonstrating the potential of hybrid perovskites for thermal management applications.

Both studies reveal that the rotational freedom of MA^+ cations is the key parameter controlling thermal transport in hybrid perovskites. In the orthorhombic phase, restricted MA^+ rotation preserves static lattice distortions, and Umklapp scattering dominates phonon resistance. In the cubic phase, dynamic MA^+ rotations generate time-dependent lattice distortions that induce resonant scattering and higher-order phonon interactions—phenomena that are extremely challenging to capture through computational modeling alone.

These findings elucidate the fundamental physics underlying the "soft" lattice dynamics of hybrid perovskites and suggest strategies for engineering thermal properties through compositional tuning or structural modifications. Understanding how organic cations mediate heat transport

may guide the design of more stable perovskite solar cells with improved thermal management, advancing their commercialization. (Reported by Yu-Chun Chuang)

*This report features the work of Jia-Kai Hu, Pai-Chun Wei and their collaborators published in Small **21**, 2408773 (2025).*

TPS 19A High-resolution Powder X-ray Diffraction
ANSTO SIKA – Cold Neutron Triple-axis Spectrometer
NIST SPINS – Spin-polarized Triple-axis Spectrometer

- Inelastic Neutron Scattering
- Hybrid Perovskites, Lattice Dynamics, Thermal Transport, Incommensurate Structures

References

1. M. Jeong, I. W. Choi, E. M. Go, Y. Cho, M. Kim, B. Lee, S. Jeong, Y. Jo, H. W. Choi, J. Lee, Science **369**, 1615 (2020).
2. Y. Guo, O. Yaffe, D. W. Paley, A. N. Beecher, T. D. Hull, G. Szpak, J. S. Owen, L. E. Brus, M. A. Pimenta, Phys. Rev. Mater. **1**, 042401 (2017).
3. W.-H. Li, C.-H. Lee, T.-Y. Ling, M.-H. Ma, P.-C. Wei, J.-H. He, C.-M. Wu, J.-C. Peng, G. Xu, Y. Zhao, Phys. Rev. Mater. **5**, 025401 (2021).
4. J.-K. Hu, Y.-J. Lee, C.-C. Wu, C.-H. Lee, C.-M. Wu, H.-C. Wu, K. Nawa, K. Kinjo, T. J. Sato, P.-C. Wei, Small **21**, 2408773 (2025).

Shining X-rays into the Heart of Catalytic Complexity

Seeing through the spinel, element-selected XAS unveils the secret physics that drive high-entropy catalysts.

In the fast-moving field of materials science, researchers are turning chaos into opportunities. A new generation of catalysts, called high-entropy catalysts (HECs), is challenging the traditional notion that simplicity leads to stability. Traditional catalysts typically rely on one or two principal elements, sometimes enhanced by dopants or supports to tailor activity or stability. By contrast, HECs are defined by the deliberate incorporation of multiple principal components—metals, oxides, nitrides, carbides, or sulfides—into a single-phase matrix. The key principle lies in maximizing configurational entropy ($\Delta S_{config} = R \ln N$), where R is a constant and N is the number of constituent elements. A high ΔS_{config} value can offset the positive enthalpy of mixing, stabilizing otherwise phase-separated systems into uniform crystalline phases. By blending more elements in different proportions, scientists are discovering materials that are not only more robust but also remarkably efficient in driving critical energy reactions. Among these, spinel (AB_2O_4), rock-salt (MO), layered (P2-type), and perovskite (ABO_3) structures are the most widely adopted for HECs as they provide a perfect balance between entropy stabilization and functional versatility. The spinel structure features an entropy-friendly lattice that supports multiple transition metals, high-temperature synthesis, and strong electrochemical stability. Within spinel HECs, this framework enhances thermodynamic stability and improves functional performance, enabling effective charge transfer, reversible redox processes, and extended durability.

Gaining insights into the local environments of spinel structures, including the atomic bonding and oxidation at different sites and electron exchange during reactions, is essential for improving catalyst design. This is where X-ray absorption spectroscopy (XAS) is utilized. Often referred to as a "fingerprint," the XAS technique enables researchers to examine specific elements in complex materials and observe their changes over time. By scanning the energy of X-rays across an element's absorption edge, scientists can identify its oxidation state, coordination geometry, and local bonding environment. This highlights the role of the XAS technique in revealing active sites, oxidation state evolution, and electronic structure modulation. Recent studies conducted this year have demonstrated the effectiveness of using XAS beamlines at the NSRRC. The studies revealed how certain metals can dynamically switch between oxidation states during oxygen evolution reactions,

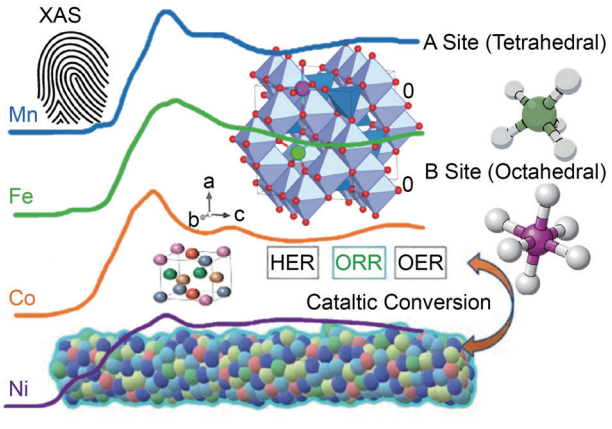

Fig. 1: An in-depth analysis of the AB_2O_4 spinel-type high-entropy catalyst utilizing element-selected XAS techniques reveals significant insights into its catalytic performance and stability.

while others maintain stability to preserve the spinel framework, as depicted in **Fig. 1**. These findings help explain why these catalysts often perform better than their single-metal counterparts.

An impressive study on spinel HECs led by Yu-Chuan Lin (National Cheng Kung University) revealed how redox-active metals enable self-regeneration in high-entropy oxides.[1] Their findings uncover the dynamic restructuring of spinel-type catalysts under redox environments in the context of CO_2 conversion. Lin's team compared two spinel systems, namely $MnFeCoNiCuO_x$ and $MnCoNiCuZnO_x$, with nearly identical configurational entropy but contrasting redox behavior. Using *in situ* XAS at the **TPS 32A** beamline, they observed that only the Fe-containing catalyst could reversibly exsolve and reincorporate Fe/Co/Ni/Cu alloy nanoparticles during alternating H_2 and CO_2 atmospheres. Conversely, when Fe was replaced by redox-inert Zn^{2+}, the catalyst became rigid and unable to form alloy nanoparticles, as shown in **Fig. 2**. The team concluded that configurational entropy alone does not guarantee catalytic adaptability; rather, the inclusion of redox-flexible cations such as Fe^{3+} is key to enabling regenerative performance. XAS analyses confirmed that $MnFeCoNiCuO_x$ possesses higher concentrations of surface oxygen vacancies and metallic alloy phases, both crucial for CO_2 activation and hydrogenation. This work not only deepens the understanding of redox-driven structural dynamics in entropy-stabilized oxides but also proposes design principles for next-generation catalysts that can self-regenerate under realistic reaction conditions. Such insights pave the way for efficient CO_2 conversion using renewable hydrogen—a cornerstone for sustainable chemical processes.

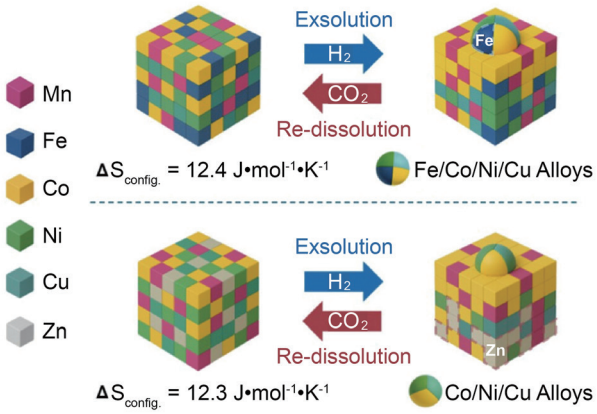

Fig. 2: Conceptual diagram of the reversible exsolution and redissolution of Fe/Co/Ni/Cu alloy NPs on $MnFeCoNiCuO_x$ and Co/Ni/Cu alloy NPs on $MnCoNiCuZnO_x$ with the change of the local coordination of Zn^{2+}. [Reproduced from Ref. 1]

Another excellent study this year, conducted by Wei Hsuan Hung (National Central University), utilized a six-element HEC (AlCoCrFeMnNi)O with the objective to create an efficient and stable oxygen evolution reaction (OER) catalyst for seawater environments.[2] This material demonstrated

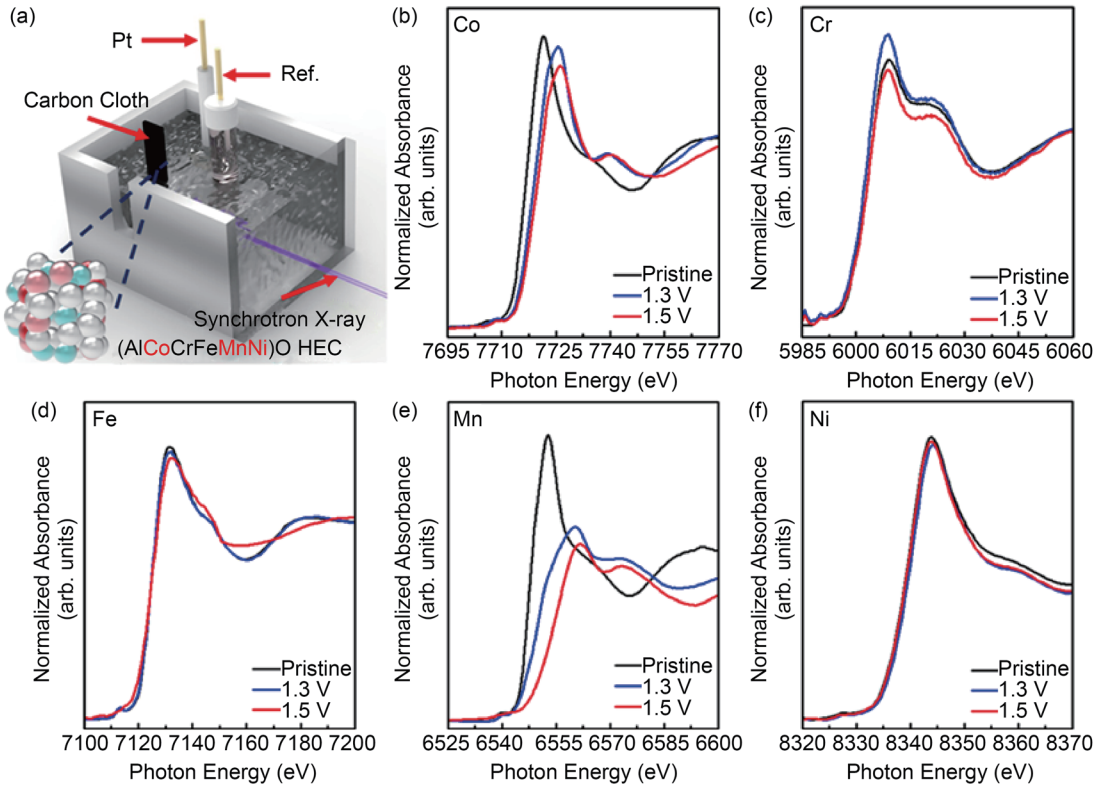

Fig. 3: (a) Setup of an electrochemical OER for *in situ* XAS measurement. *In situ* (b)Co, (c) Cr, (d) Fe, (e) Mn, and (f) Ni K-edge XAS spectra of (AlCoCrFeMnNi)O HEC powder. [Reproduced from Ref. 2]

remarkable performance, achieving an onset voltage for oxygen evolution as low as 1.47 V vs. reversible hydrogen electrode (RHE). More significantly, the (AlCoCrFeMnNi)O HEC successfully operated stably in seawater for 1,000 hours under a constant current density of 100 mA/cm^2, demonstrating extraordinary stability in the salt-rich environment. *In situ* XAS carried out during OER with varying applied voltages at **TPS 44A** beamline revealed that Co and Mn underwent OER-dependent oxidation (valence changes), evidenced by shifts in their edge-jump regions toward higher photon energy, as shown in **Fig. 3**. This mechanism is known as the adsorbate evolution mechanism, where the active metal binds to the reaction intermediate, resulting in an increased negative charge. Meanwhile, a decrease in coordination number for both Co and Ni occurs without a corresponding increase in oxidation state, where oxygen atoms detach from the lattice to form an oxygen vacancy. The stabilizing elements Al, Cr, and Fe did not show significant valence changes during the OER. Their roles are critical for ensuring longevity. The absence of Fe, for example, leads to the loss of synergistic influence of the spinel phase.

These spinel HECs are being explored for CO_2 reduction, water splitting, and next-generation catalysts, offering potential pathways to cleaner energy technologies. Yet, without tools like XAS, their true potential would remain hidden behind a fog of atomic disorder. In CO_2 conversion, *in situ* XAS revealed that redox-flexible cations like Fe^{3+} enable a reversible "breathing" mechanism that enhances performance. For seawater splitting, XAS showed that active metals (Co and Mn) switch oxidation states while stabilizing elements (Al, Cr, Fe) maintain the high-entropy structure. This insight transforms HECs from randomness into a balanced atomic ensemble for a cleaner, more efficient future. (Reported by Chi-Liang Chen of the NSRRC and Yu-Chuan Lin of National Cheng Kung University)

This report features the work of Yu-Chuan Lin and his collaborators published in ACS Appl. Mater. Interfaces ***17****, 52315 (2025); and the work of Wei Hsuan Hung and his collaborators published in Sustain. Mater. Technol.* ***45****, e01515 (2025).*

TPS 32A Tender X-ray Absorption Spectroscopy
TPS 44A Quick-scanning X-ray Absorption Spectroscopy

- XAS
- Spinel, Materials Science, Green Sustainable Chemical Process, Water Splitting

References

1. P.-T. Chou, C.-C. Kuo, P.-Y. Peng, Y.-R. Lu, C.-L. Chen, Y.-C. Lin, ACS Appl. Mater. Interfaces **17**, 52315 (2025).
2. I-C. Chiu, C.-Y. Chiang, H.-Y. Chang, C.-T. Li, H.-Y. Chi, H.-C. Huang, P. Chang, Y.-T. Wang, R. Lee, I-Y. Tsao, C.-L. Chiang, B. K. Chang, Y.-G. Lin, W. H. Hung, Sustain. Mater. Technol. **45**, e01515 (2025).

(Photo)electrochemical H_2O_2 Sensing Platform for Future Application in Cancer Diagnosis

The controllable synthesis of anatase–rutile TiO_2 has been developed, which exhibits enhanced (photo)electrocatalytic activity for the monitoring of hydrogen peroxide under visible light, presenting potential applications in cancer diagnosis.

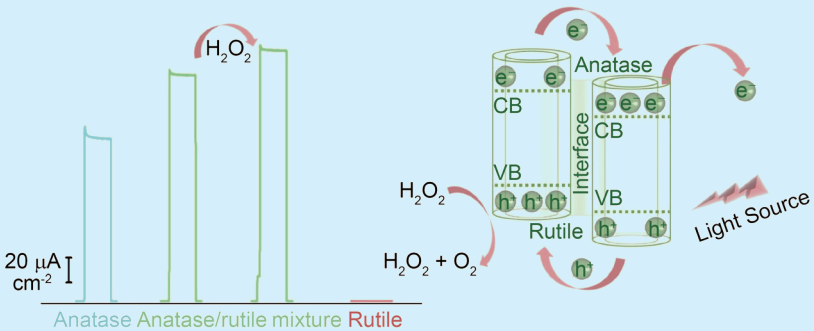

Fig. 1: Schematic illustration of photoelectrochemical H_2O_2 sensing based on the anatase–rutile phase transformation on TiO_2 supports. [Reproduced from Ref. 1]

Reactive oxygen species (ROS), such as superoxide ($O_2^{\cdot-}$), hydroxyl radicals (OH·), and hydrogen peroxide (H_2O_2), play essential roles in metabolic regulation and immune responses *via* nicotinamide adenine dinucleotide phosphate (NADPH) oxidase activation. While ROS are necessary for cellular homeostasis, excessive levels lead to protein

and lipid oxidation, DNA damage, and oxidative stress, all of which contribute to carcinogenesis. Among ROS, H_2O_2 is moderately reactive yet sufficiently stable to diffuse across membranes and reach the nucleus, where it can cause oxidative DNA damage. Its strong association with tumor initiation and progression highlights the need for sensitive and reliable H_2O_2 detection strategies.

Multiple analytical methods—including fluorescence, chemiluminescence, colorimetry, electrochemistry, and photoelectrochemistry (PEC)—have been developed for H_2O_2 sensing. PEC has attracted significant interest because of its high sensitivity, low background noise, and the separation of optical excitation from electrical detection. In PEC systems, photoactive materials generate electron–hole pairs under illumination, which drive redox reactions with probe molecules and produce measurable photocurrents. Therefore, optimizing photoactive materials is crucial for achieving high PEC performance.

Titanium dioxide (TiO_2) is one of the most widely used photoelectrode materials due to its stability, low cost, and environmental friendliness. However, its wide bandgap and limited charge transport hinder performance. Mixed-phase TiO_2, particularly anatase–rutile heterostructures, enhances charge separation through stable phase boundaries and defect-rich interfaces with oxygen vacancies and Ti^{3+} states. These characteristics improve carrier mobility and suppress recombination, significantly increasing PEC activity (**Fig. 1**).

Nanostructured TiO_2 significantly improves performance by increasing the active surface area and enhancing mass transport. One-dimensional (1D) TiO_2 architectures, such as nanotubes, are particularly beneficial due to their efficient electron pathways. Electrochemical anodization is widely used to fabricate ordered TiO_2 nanotubes. To mitigate environmental concerns related to fluoride electrolytes, recent studies have utilized fluoride-free phosphate, sulfate, and nitrate electrolytes, in which nanotube growth is controlled by the oxygen bubble mold mechanism.

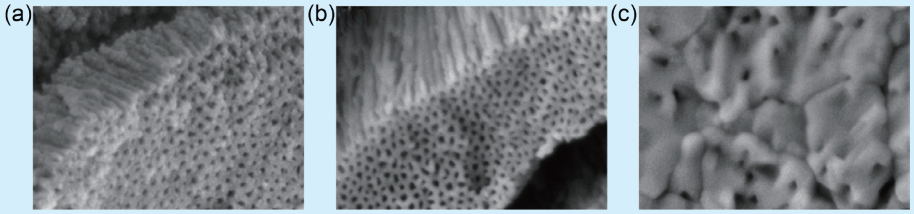

Fig. 2: FESEM images of (a) anatase, (b) anatase–rutile mixture, and (c) rutile TiO_2 supports. [Reproduced from Ref. 1]

To fully understand sensing behavior, synchrotron-based X-ray spectroscopies—including X-ray absorption spectroscopy (XAS) at **TLS 20A1**, wide-angle X-ray scattering (WAXS) at **TLS 23A1**, and X-ray excited optical luminescence (XEOL) at **TPS 23A**—analyze morphological, chemical, and electronic changes, offering key insights into structure–reactivity relationships in PEC systems for H_2O_2 detection.

Han-Wei Chang (National United University) demonstrated that 1D TiO_2 nanotubes—anatase (400 °C), anatase–rutile mixture (600 °C), and rutile (800 °C) TiO_2 supports—synthesized *via* fluoride-free electrochemical anodization and subsequent thermal annealing, show strong potential as PEC catalysts for H_2O_2 sensing in human serum. The TiO_2 supports were extensively characterized using Field Emission Scanning Electron Microscopy (FESEM) and synchrotron-based techniques, including XAS, WAXS, and XEOL, at the NSRRC, Taiwan. These analyses revealed that annealing enables precise control over the anatase–rutile phase composition, Ti^{3+}/Ti^{4+} distribution, and oxygen vacancy concentration, all of which significantly influence PEC activity. FESEM images (**Fig. 2**) show well-aligned, vertically oriented nanotube arrays several micrometers long with nanometer-scale inner diameters. The nanotubes form through the oxygen bubble mold mechanism, governed by the interplay of ionic and electronic currents during anodization. Heat treatment at increasing temperatures transformed the TiO_2 crystalline structures and tailored their surface properties. The optimized nanotube arrays, featuring enhanced charge transport and abundant active sites, exhibited superior PEC performance for H_2O_2 detection.

To investigate the structural evolution of anodized Ti-based samples annealed at different temperatures, WAXS (**TLS 23A1**), XEOL (**TPS 23A**), and XAS (**TLS 20A1**) analyses were performed. WAXS was used to examine phase transitions and crystal structure development. Grain sizes were estimated using the Scherrer equation. As shown in **Fig. 3(a)**, reference patterns for anatase and rutile TiO_2 were included for peak identification. All samples exhibited diffraction peaks corresponding to metallic Ti, reflecting the underlying Ti substrate. Additional peaks appearing between 400 and 600 °C indicate the formation of crystalline anatase TiO_2, with peak intensities increasing with temperature, confirming enhanced crystallinity and phase stability. Weak rutile peaks emerge at 600 °C, demonstrating the onset of the anatase–rutile transformation. At 800 °C, the complete disappearance

of anatase peaks and the dominance of rutile reflections confirm a full phase transition, consistent with morphological changes observed in FESEM.

XEOL was used to analyze defect-related optical emissions during phase transformation. XEOL detects luminescence generated by X-ray excitation, providing sensitivity to deep-level defects. As shown in **Fig. 3(b)**, anatase and mixed-phase TiO_2 samples exhibit a green emission at ~501 nm (2.48 eV), attributed to oxygen vacancies and hydroxyl-related defect states. Mixed anatase–rutile samples also show a broad near-infrared emission centered at 855 nm (1.45 eV), associated with deep traps—likely originating from Ti interstitials or oxygen vacancies that reduce Ti ions. Multiple resonances in this band suggest strong exciton–phonon coupling. At 800 °C, where rutile is predominant, defect-related emissions are greatly suppressed, indicating a lower defect density and the absence of anatase-related luminescence.

XAS at the Ti L-edge and O K-edge was performed to investigate annealing-induced changes in surface electronic structure. **Figure 3(c)** presents Ti $L_{2,3}$-edge spectra, where the L_3–eg doublet (peaks 4a and 4b) is a sensitive indicator of crystal phase. Anatase samples exhibit a strong low-energy 4a peak and a weaker 4b shoulder. As annealing temperature increases, the relative intensities shift, indicating a gradual transformation from anatase to rutile. At 600 °C, mixed-phase samples maintain an anatase-dominant profile, while at 800 °C, the inversion of the 4a/4b intensity ratio confirms a rutile-dominant surface.

Figure 3(d) shows the O K-edge XAS spectra. Anatase samples display characteristic pre-edge peaks (4c and 4d) corresponding to O 2p–Ti 3d hybridized states. Rutile samples exhibit clear splitting of the 4f peak into two components ($4f_1$ and $4f_2$), along with a blue shift of the 4e peak, enabling reliable differentiation between phases. Mixed anatase–rutile samples annealed at ~600 °C display partial splitting and shifting, confirming the coexistence of both phases. At 800 °C, the absence of anatase features indicates complete conversion to rutile, consistent with Ti $L_{2,3}$-edge results.

Collectively, WAXS, XEOL, and XAS show that anodized TiO_2 remains mainly anatase up to ~600 °C, partially transforms into an anatase–rutile mixture at 600 °C, and fully converts to rutile at 800 °C. This controllable phase evolution directly affects the electronic structure and defect landscape of TiO_2, offering tunable properties essential for optimizing its performance in photoelectrochemical sensing applications. (Reported by Han-Wei Chang, National United University)

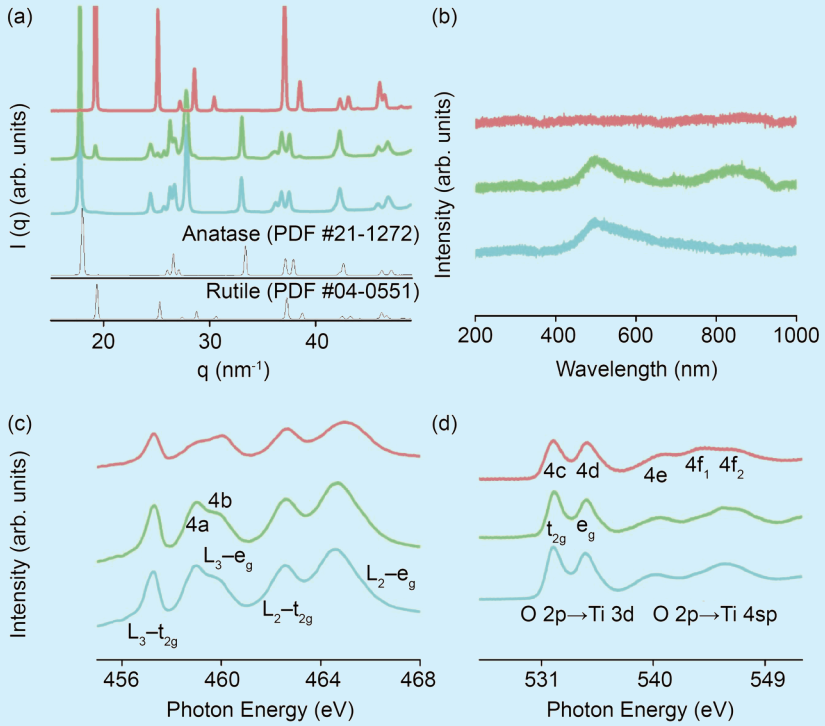

Fig. 3: (a) WAXS profiles, (b) XEOL spectra, (c) Ti L-edge XAS spectra, and (d) O K-edge XAS spectra of anatase (blue line), anatase–rutile mixture (green line), and rutile TiO_2 supports (red line). [Reproduced from Ref. 1]

This report features the work of Han-Wei Chang and his collaborators published in Surf. Interf. ***74****, 107719 (2025).*

TPS 23A X-ray Nanoprobe
- XEOL
- Materials Science, Chemistry

TLS 20A1 XAS
- XAS
- Materials Science, Chemistry

TLS 23A1 Small/Wide Angle X-ray Scattering
- WAXS
- Materials Science, Chemistry

Reference

1. Y.-H. Lin, C.-C. Chen, Y.-H. Chen, Y.-S. Huang, B.-H. Lin, U-S. Jeng, S.-C. Haw, C.-J. Su, L.-Y. Chang, H.-H. Hsieh, H.-W. Chang, Surf. Interf. **74**, 107719 (2025).